*J. Fluid Mech.* (2012), *vol.* 694, *pp.* 371–398.  
doi:10.1017/jfm.2011.552

# Intermittency and inertial particle entrainment at a turbulent interface: the effect of the large-scale eddies

**G. H. Good[1], S. Gerashchenko[1]‡ and Z. Warhaft[1,2]†**

[1] Sibley School of Mechanical and Aerospace Engineering, Cornell University, Ithaca, NY 14853, USA and International Collaboration for Turbulence Research

[2] Atkinson Center for a Sustainable Future, Cornell University, Ithaca, NY 14853, USA

(Received 22 February 2011; revised 4 December 2011; accepted 11 December 2011; first published online 3 February 2012)

We present measurements of mean and conditional number densities, radial distribution functions (r.d.f.s), velocities and accelerations of sub-Kolmogorov-scale water droplets entraining at a shearless turbulence–turbulence interface (TTI) and a turbulence–non-turbulence interface (TNI). We thus look at statistics of an inhomogeneous inertial particle field in both homogeneous and inhomogeneous turbulence. As in a previous communication (Gerashchenko, Good & Warhaft *J. Fluid Mech.*, vol. 818, 2011, pp. 293–303), an active grid produces high-Reynolds number turbulence ($Re_\lambda = 275$) on either one or both sides of a splitter plate in a wind tunnel. Sprays seed droplets on one side of the splitter plate, while screens dampen turbulence in the adjacent flow for the TNI. Gravitational and inertial effects are isolated by turning of the apparatus with respect to gravity. We parameterize the droplets under homogeneous conditions, where it is demonstrated that both the sweeping and loitering effects on the droplet settling velocities are present. In the inhomogeneous conditions, we show that the droplets are entrained in bulk, resulting in large-scale clusters and preserving the droplet-ambient conditions of the seeded side of the flows.

**Key words:** intermittency, particle/fluid flows, turbulent mixing

## 1. Introduction

Entrainment, the means by which turbulent flows spread and grow, is fundamental to all turbulent flows with interfaces, be they interfaces with a laminar flow, or another turbulent flow with different properties (e.g. length and energy scales). The subject has been extensively studied in traditional turbulent shear flows (e.g. Townsend 1976) for both the velocity and passive scalar fields, and for reactions (e.g. Broadwell & Breidenthal 1982). There have been entrainment studies of turbulent plumes (Turner 1986), the atmospheric boundary layer (Deardorff 1974), stable density interfaces (Kantha, Phillips & Azad 1977) and clouds (Shaw 2003; Andrejczuk *et al.* 2004). Yet, while a significant amount of numerical and experimental work has been done

† Email address for correspondence: zw16@cornell.edu

‡ Present address: Now with the P-23 Extreme Fluids Team, Los Alamos National Laboratory, Los Alamos, NM 87545, USA.

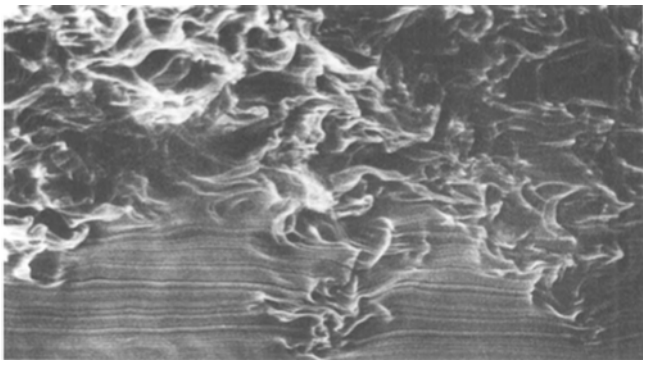

FIGURE 1. Smoke-wire image from Jayesh & Warhaft (1994) demonstrating large-scale intermittency at the interface between a highly turbulent and relatively quiescent flow. This is like the TNI case in the present work, albeit in Jayesh & Warhaft (1994) the flow was created using a combination of a passive grid and damping screens, and there were no droplets.

for the above-mentioned cases, comparatively little is known about the entrainment of inertial particles, particles which are heavier than their surrounding fluid, such as the water droplets in clouds, the droplets formed by spray injectors, or the soot particles formed due to incomplete combustion in diesel engines.

While detailed knowledge is lacking on the entrainment of inertial particles, considerable work has been done on the effects of turbulence on their settling velocities (e.g. Murray 1970; Nielsen 1993; Wang & Maxey 1993; Aliseda *et al.* 2002), their small-scale clustering in isotropic conditions (Squires & Eaton 1991; Wang & Maxey 1993; Sundaram & Collins 1997; Wood, Hwang & Eaton 2005; Saw *et al.* 2008; Salazar *et al.* 2008), their inertial-scale density fluctuations in isotropic conditions (Bec *et al.* 2007) and their mixing and preferential concentration in complex flows (Lázaro & Lasheras 1989; Longmire & Eaton 1992). It is our objective here to extend these investigations to explore the effects of entrainment on inertial particle fields. Our study follows on from the earlier experiments of Gerashchenko, Good & Warhaft (2011), here forth denoted as GGW.

The smoke-wire photo in figure 1 illustrates the type of entrainment process we are concerned with. The photo shows no droplets, but rather a turbulent flow (above) which entrains fluid from the adjacent, quiescent flow below it. At the interface, the velocity field is intermittent at the large scales. We ask: what is the case when the turbulent side of the flow is droplet-laden, like at the boundary of a cloud? Might the particles entrain and cluster at the large scales? What is the role of gravity and inertia, and how will the entrainment affect the particle dynamics, size and spatial distributions? How dependent might such large-scale clustering be on the nature of the entraining velocity field? That is, what is the difference in the clustering characteristics of a particle field which has been entrained from a droplet-laden, turbulent region into a dry region which is in one case non-turbulent (figure 1) and in another having the same turbulence as the droplet-laden fluid?

We examine these questions by looking at two shearless interfaces, a homogeneous, turbulence–turbulence interface (TTI), and a turbulence–non-turbulence interface (TNI), similar to that in figure 1. In our flows, water droplets are injected into intense grid turbulence on one side of a splitter plate; the adjacent, droplet-free flow is either equally turbulent or nearly laminar. Downstream of the splitter plate an interface forms. In the preliminary study of GGW, the mean particle density and size profiles were

reported, as was some information on the mean particle velocities. Gravitational and inertial effects were isolated by turning the apparatus with respect to the gravitational field. It was shown that in the absence of gravity, the droplet size distribution did not change across the interfaces. This means firstly that the large scales (which could not distinguish between the variously sized droplets based on inertia) are responsible for the entrainment, and secondly, that the particle-laden side of the flow is entrained in bulk, such that the air ambient to the droplets remains saturated and they do not evaporate. When gravity was directed across the interfaces in GGW, the droplets were selectively transported based on their size. The TTI droplet mean number density profiles were error functions, while the TNI profiles indicated a sharper fall-off in the droplet mean number density. The mean velocity measurements of the particles showed enhanced bulk particle transport for the TTI as compared with the TNI, but they were unable to discern the effects of gravity.

In the present study, we use the same flow facility as in GGW to investigate the entrainment mechanism and address the questions we have posed above. Here, we have expanded the use of the word 'entrainment', which may typically describe the drawing in of quiescent fluid by a turbulent flow (like at the TNI, as in figure 1). We expand its use to include the entrainment of particle-free fluid by a particle-laden flow with even the same turbulence (as in the TTI), since we will show that the effect of the large eddies on the particle field has much in common with the classical entrainment situation. To this end, we examine the particle velocity field, including the higher-order moments, the particle radial distribution functions (r.d.f.s), conditional statistics and acceleration measurements. Apart from background information and a re-examination of the droplet mean number density data shown in GGW, all of the results presented here are new.

The outline of the paper is as follows: in § 2 we describe the experimental apparatus. This is followed by the results section. We first provide documentation on the velocity field, including higher-order moments and spectra, before describing the properties of the droplets in homogeneous conditions. We show that the settling speeds of the polydispersed droplets may be either enhanced or reduced with respect to their Stokes velocities, due to the competing effects of the turbulence on particle settling (Nielsen 1993), as discussed in § 3.2.2. After parameterizing the droplets, we turn our attention to the inhomogeneous particle fields of the droplet mixing layers, and investigate their mean number density profiles, r.d.f.s (defined in § 3.3.2) and some conditional statistics. This is followed by an analysis of the droplet velocity and acceleration data. In particular, we discern the subtle effects of gravity and inertia on the particle field, and show that within the intermittent, large-scale clusters which contain most of the droplets in the initially dry sides of the flows, the particle and fluid conditions are similar to those in the droplet-laden side.

## 2. Experimental set-up

The experimental set-up is the same as in GGW. It allows for six different configurations: two flows with three gravity cases each. The wind tunnel is divided with a splitter plate and water droplets are injected via sprays into strongly turbulent flow on one side (figure 2), downstream of an active grid (Mydlarski & Warhaft 1996; Kang & Meneveau 2008). The adjacent, droplet-free flow is made either turbulent or non-turbulent by means of the same active grid or damping screens. Downstream of the 2.5 m splitter plate there is either a TTI or TNI, and a mixing layer develops. The mixing layer is kept shearless in both cases, such that only turbulence–turbulence

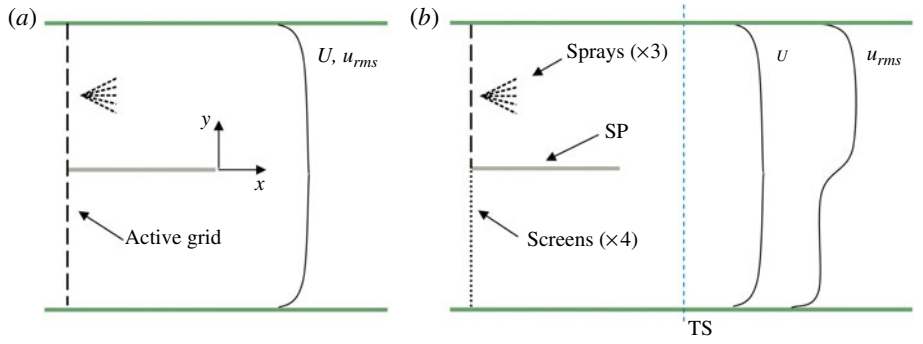


FIGURE 2. (Colour online available at journals.cambridge.org/flm) Sketches of the TTI (*a*) and TNI (*b*) flow apparatus. For the sketches, the $g+$, $g-$ and $g0$ cases are with gravity directed down, up and into the page, respectively. The active grid (black dashed line) has mesh length 10 cm, while the screens (dotted line) have mesh length 2 mm. Sprays inject droplets into the turbulent side of the flows. The splitter plate (SP) is 2.5 m long and the test section (TS), where the bulk of the measurements are done, is 1.17 m beyond its trailing edge.

interactions are present (Veeravalli & Warhaft 1989; GGW). The sprays consist of three 1 mm diameter coflowing air and water nozzles, placed 5 cm downstream of the active grid (Gerashchenko *et al.* 2008). As shown in Gerashchenko *et al.* (2008), by the time the droplets reach the test section the effect of excess momentum produced by the sprays is diluted such that no abnormalities in the mean profiles are observed. The flow configurations (figure 2) may be rotated by 90 and 180° such that the splitter plate is horizontal and gravity either aids ($g+$) or impedes ($g-$) droplet transport into the adjacent flow, or is vertical such that gravity is orthogonal to the mixing layer ($g0$).

The longitudinal and transverse coordinates are defined as $x$ and $y$, with the origin at the splitter plate trailing edge; positive $y$ values denote distance into the droplet injection region. The test section is at $x = 1.17$ m, which is 0.7 large-eddy turnover times from the splitter plate trailing edge. The mean tunnel velocity is $U = 2.15$ m s$^{-1}$, with fluctuating longitudinal and transverse components defined as $u$ and $v$, respectively. The negative of the transverse velocity, $-v$, will be presented in figures such that mean transport across the mixing layers is seen as positive. Fluid velocity components were measured using a hot-wire anemometer X-array with 3.05 μm tungsten wires (Mydlarski & Warhaft 1996). Droplet size, velocity and linear (one-dimensional, 1D) density statistics were measured with a two-component Phase Doppler Particle Analyzer (PDPA, TSI Inc.). Within the droplet-laden side of the flows, the air is saturated or nearly saturated and calculations show evaporative effects to be negligible. Droplet size distribution measurements at both the initial condition and test section confirm this. Given the flight time of the particles to the test section, calculations do show that a droplet in the ambient conditions of the dry side of the flows should experience severe evaporative effects, altering their numbers and size distribution. The $g0$ droplet size profiles of GGW showed this not to be the case, however, and the reasons for this are the purview of the present study. Calculations also show the temperature differences across the interface to be too small to result in buoyancy effects. The small PDPA measurement volume (300 μm × 50 μm × 50 μm) and seeding density ($m_{water}/m_{air} \approx 10^{-5}$) allow accurate velocity, size and number density measurements (Gerashchenko *et al.* 2008). PDPA and hot-wire measurements

confirm that the particle and velocity fields are statistically homogeneous in the $z$ direction, that is, parallel to the splitter plate trailing edge. The number of PDPA droplet measurements depended on the location, but they were generally of order $10^4$ for the number density and $10^5$ for the velocity data. The difference is due to the periodic need for number density reference measurements due to long-time fluctuations in the spray output.

Some droplet acceleration measurements are also shown. These were performed using a unique, Lagrangian particle tracking system which utilizes a high-speed camera (Phantom v7.1) attached to a precision, linearly translating sled developed by Armann Gylfason (Ayyalasomayajula *et al.* 2006). The sled is pneumatically driven at the mean flow speed in order to track particles over many frames. The sled moves outside of and parallel to the wind tunnel's glass walls. The camera delivered 8000 frames per second and its resolution was 512 $\times$ 512 pixels. The particles were illuminated by means of forward scattering from a laser beam (Nd-YAG, 20 W, pulse width 120 ns, 40 kHz pulse) connected to the sled via a fibre optic cable and projected in the Lagrangian frame. The forward scattering was achieved by reflection of the beam off of a mirror on the far wall of the tunnel, as in Gerashchenko *et al.* (2008). (For some measurements, a periscope assembly was introduced to the sled to measure at various $y$ locations in the gravitational cases, where the splitter plate is horizontal.) The particles were tracked over a distance of 50 cm, centred at the test section, through which the sled velocity is constant. This large measurement window (compared with the PDPA measurement volume) is necessary in order to achieve adequate particle tracks for determining accelerations statistics. Each movie is individually postprocessed by subtracting the minimum observed brightness for each pixel. The particle tracking algorithm developed by the Bodenschatz group (Voth *et al.* 2002; Ouellette *et al.* 2006) was used and the accelerations were calculated by the convolution of the measured particle tracks with a Gaussian smoothing and differentiating filter (Mordant, Crawford & Bodenschatz 2004). The acceleration data shown are based on individual droplet acceleration measurements numbering of the order of $10^6$.

## 3. Results

In this section, we characterize the air flows with hot-wire measurements, and this is followed by the droplet data, which were measured using both PDPA and Lagrangian particle tracking techniques.

### 3.1. *The velocity field*

We begin with velocity profiles of the TTI and TNI and use these to define the dominant turbulence scales. This is followed by an examination of the velocity spectra and the fluid velocity moments, the latter of which describe large-scale intermittency in the flows.

#### 3.1.1. *The turbulence interfaces*

Longitudinal, $u$, and transverse, $v$, velocity root mean square (r.m.s.) components are shown in figure 3, as is the turbulence dissipation rate, calculated as $\epsilon \approx 15(\nu/U^2)\langle(\partial u/\partial t)^2\rangle$ based on Taylor's hypothesis, where $\nu$ is the kinematic viscosity of air. The values are nearly constant across the TTI, while for the TNI, as shown by Veeravalli & Warhaft (1989), the profiles are approximately error functions. The turbulent kinetic energy ($k \approx (1/2)(u_{rms}^2 + 2 \cdot v_{rms}^2)$) ratio across the TNI is approximately 30, and the interface is thus dominated by the highly turbulent side of the flow and

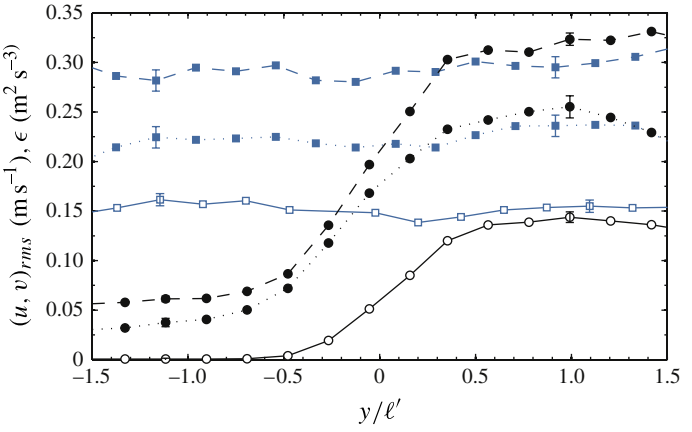


FIGURE 3. (Colour online) Hot-wire profiles of the velocity r.m.s. (filled symbols) and dissipation (open symbols) at the test section for the TTI (squares) and TNI (circles). The $u$ and $v$ velocity r.m.s. components have dashed and dotted lines, respectively. To avoid clutter, error bars are shown at representative locations only.

| $Re'_\lambda$ | $\epsilon'$ (m$^2$ s$^{-3}$) | $U$ (m s$^{-1}$) | $u'_{rms}$ (m s$^{-1}$) | $v'_{rms}$ (m s$^{-1}$) | T.I.$'$ (%) |
|---|---|---|---|---|---|
| 275(12) | 0.138(0.006) | 2.15(0.05) | 0.31(0.01) | 0.24(0.01) | 14.4(0.8) |
| $\lambda'$ (cm) | $\eta'$ (mm) | $\tau'_\eta$ (ms) | $u'_\eta$ (cm s$^{-1}$) | $\ell'$ (cm) | $\tau'_\ell$ (s) |
| 1.3(0.04) | 0.397(0.006) | 10.5(0.3) | 3.8(0.6) | 24(2) | 0.8(0.09) |

TABLE 1. Flow Parameters in the TNI high turbulence, or equivalently, the TTI turbulence, as signified by the primes. The mean velocity does not vary across the shearless interfaces. The Taylor microscale and its Reynolds number are defined as $\lambda \equiv \sqrt{15\nu u'^2_{rms}/\epsilon}$ and $Re_\lambda \equiv u_{rms}\lambda/\nu$. The turbulence intensity, T.I.$'$ is defined as $u'_{rms}/U$.

its scales (GGW). The transverse coordinate, $y$, is normalized by the integral length scale, $\ell'$, as determined from the longitudinal velocity spectra in the TTI (or the high-turbulence side of the TNI). Table 1 shows characteristic flow parameters at the test section, as measured in the high-energy turbulence of the TTI and the high-turbulence side of the TNI. Primes denote the (constant) values in this turbulence. The turbulence anisotropy, $u'_{rms}/v'_{rms}$, is around 1.3, consistent with Mydlarski & Warhaft (1996). The Kolmogorov eddy velocity and time microscales are defined as $u_\eta \equiv (\nu\epsilon)^{1/4}$ and $\tau_\eta \equiv \sqrt{\nu/\epsilon}$.

3.1.2. *The velocity spectra*

Figure 4(*a*) shows the longitudinal velocity power spectra, $F_{11}(\kappa)$, across the TNI, normalized with local dissipation scaling. Energy spectra, $\kappa F_{11}(\kappa)$, are shown in figure 4(*b*), normalized by the high-turbulence side large-eddy scales. The spectra locations are denoted in the figure 4(*b*) inset, which also shows the variation of the mean dissipation length scale, $\eta \equiv (\nu^3/\epsilon)^{1/4}$. As the TNI is traversed from the high- to low-turbulence sides, the energy decreases. (This is most evident in figure 4*b*.) However, there is some low-energy, large-scale noise on the low-turbulence side,

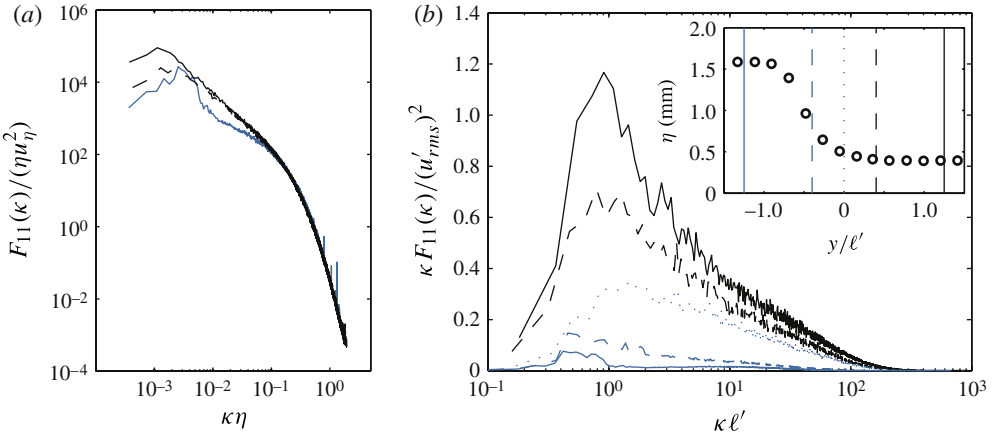


FIGURE 4. (Colour online) Power (*a*) and energy spectra (*b*) for the TNI, normalized with local dissipation scaling (*a*) and the high-turbulence side large-eddy scales (*b*). The inset shows the profile of $\eta$ at the test section; vertical lines illustrate the locations of the spectra in the main figures ($y/\ell' \approx \pm 1.25, \pm 0.4, 0$), with lines from left to right in the inset corresponding to spectra from bottom to top in the figures. Only three power spectra are shown to avoid clutter from the collapse ($y/\ell' \approx -1.25, 0.4, 1.25$).

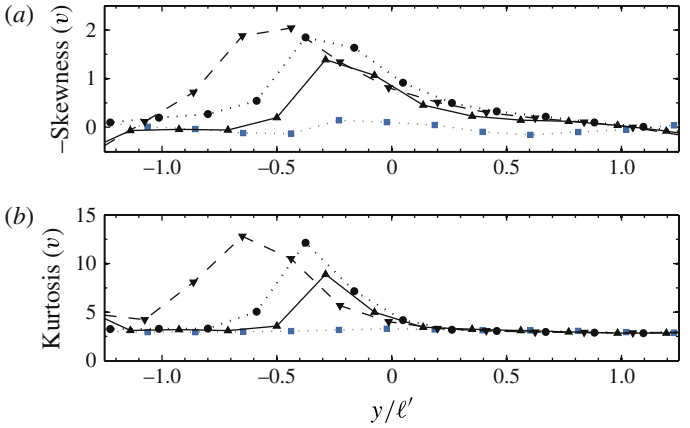


FIGURE 5. (Colour online) Profiles of the velocity skewness (*a*) and kurtosis (*b*). Squares are TTI profiles at the test section. TNI profiles upstream ($t/\tau_{\ell'} \approx 0.4$, $x = 0.7$ m), downstream ($t/\tau_{\ell'} \approx 1.1$, $x = 1.8$ m) and at the test section ($t/\tau_{\ell'} \approx 0.7$, $x = 1.20$ m) are denoted by upward- and downward-pointing triangles and circles, respectively.

present also at the initial condition. Its low energy suggests that it does not play a significant role in the turbulence dynamics.

### 3.1.3. *Large-scale intermittency and 'bursting'*

Figure 5 shows the normalized third and fourth fluid fluctuating velocity moments. For the TTI case these are close to Gaussian, as expected, while for the TNI case the values become strongly non-Gaussian and peak in the low-turbulence region. Peaks of skewness and kurtosis coincide and their displacement grows with the mixing layer, as does $\ell$. There is additionally slight but monotonic growth in the peak magnitudes of

| Droplet group | $\langle d \rangle$ (μm) | $\langle St_{\eta'} \rangle$ | $\langle Sv_{\eta'} \rangle$ | $\langle St_{\ell'} \rangle$ | $\langle Sv_{\ell'} \rangle$ |
|---|---|---|---|---|---|
| Small | 13.8 (0.3) | 0.061 (0.002) | 0.17 (0.026) | $8\ (0.9) \times 10^{-4}$ | 0.026 (0.001) |
| Intermediate | 27.2 (0.3) | 0.225 (0.006) | 0.61 (0.01) | $3\ (0.3) \times 10^{-3}$ | 0.096 (0.004) |
| Large | 51.2 (0.5) | 0.81 (0.02) | 2.2 (0.3) | 0.011 (0.001) | 0.35 (0.01) |
| All | 22.7 (0.7) | 0.2 (0.03) | 0.54 (0.01) | $2.8\ (0.1) \times 10^{-3}$ | 0.07 (0.002) |

TABLE 2. Droplet parameters in the injection side of the flows. Droplets with $d \leqslant 20$, $20 \leqslant d \leqslant 40$ and $d \geqslant 40$ μm belong to the small, intermediate and large droplet groups, respectively.

both the skewness and kurtosis downstream of the splitter plate. At the test section the peak location is $y/\ell' \approx -1/3$, where intermittent, large-scale turbulent 'bursts' penetrate into the adjacent, quiescent flow, resulting in the strong departure from Gaussian statistics (GGW; Veeravalli & Warhaft 1989). The bursting events dominate the low-turbulence-side velocity moments. As referred to in the introduction, figure 1 (from Jayesh & Warhaft 1994) shows a smoke-wire image of a multi-scale interface between a very turbulent and relatively quiescent flow generated by a passive grid and damping screens in a wind tunnel. The interface is similar to the TNI. The fluid within the interface-penetrating, large-scale 'bursts' is quite distinct from that in the quiescent region and appears to have the same turbulence characteristics as the flow above. In both the TTI and TNI, it is expected that the large scales which penetrate the interfaces are also particle-laden and will result in large-scale droplet clusters. (While such 'bursts' for the TTI are indistinguishable in the velocity field, we show that they are distinguishable by their droplet content.) The role of the large scales and their intermittency in the droplet entrainment mechanisms for the TTI and TNI will be discussed in §§ 3.3–3.5.

### 3.2. *The droplets in homogeneous conditions*

Here, we describe the droplet size distribution as measured far into the seeded side of the flows at the test section ($y/\ell' \approx 1$). We call this the homogeneous region, as it has neither gradients in the turbulence mean quantities nor in the droplet mean number density. The primed values of tables 1 and 2 apply for all data here. The relevant droplet parameters are discussed, as is the resulting bifurcation in settling effects, whereby the turbulence enhances the settling of the small droplets while diminishing that of the large droplets as compared with their Stokes velocities.

#### 3.2.1. *The droplet size distribution*

Figure 6 shows the droplet size (diameter, $d$) distribution in the homogeneous region. For the purposes of the present study the distribution has been conditioned primarily into two groups, $d \leqslant 20$ μm and $d \geqslant 40$ μm, here forth referred to as the small and large droplet groups, respectively (delineated in figure 6). The droplet group Stokes and settling parameters are listed in table 2, and are defined as $St_\eta \equiv \tau_p/\tau_\eta$ and $Sv_\eta \equiv \tau_p g/u_\eta$ for the Kolmogorov microscales, and as $St_\ell \equiv \tau_p/\tau_\ell$ and $Sv_\ell \equiv \tau_p g/v_{rms}$ for the large scales of the turbulence, where the particle response time $\tau_p \equiv \rho_p \langle d^2 \rangle / 18\mu$ and $\tau_\ell \equiv \ell/u_{rms}$. We note that while the full droplet size distribution can vary strongly as a function of $y$ in the gravitational cases (due to the selective transport of the droplets, GGW), the variation is weak within the subdistributions presented here. Both the large- and small-scale settling parameters, $Sv_{\ell'}$ and $Sv_{\eta'}$, respectively (table 2), have order one values for the large droplets

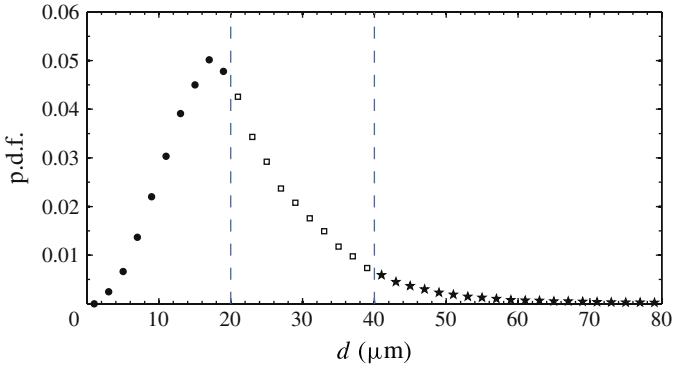


FIGURE 6. (Colour online) Normalized droplet diameter probability distribution as measured in the droplet bulk ($y/\ell' \approx 1$) at the test section. Circles, squares and stars represent the small, intermediate and large droplet groups, respectively, separated by dashed lines. This smoother p.d.f. was measured under nominally the same conditions as that shown in GGW, but is based on substantially longer data sets consisting of hundreds of thousands rather than tens of thousands of measurements.

and comparatively small values for the small droplets. The range of $St_{\eta'}$ values is similarly comprehensive; $St_{\ell'}$, however, is very small for all droplets, and so we do not anticipate that the large scales of the flow may effectively discriminate between the variously sized droplets due to their inertia.

3.2.2. *Droplet settling*

A number of mechanisms exist by which small, heavy particles may have their settling velocities enhanced or reduced in turbulent flows, and this requires some background. Settling enhancement may be facilitated via mass loading (Aliseda *et al.* 2002) or more generally via the 'sweeping' or 'fast-tracking' mechanism, by which falling particles show preference for the downward-sweeping sides of eddies. This mechanism has been well-documented in experiments (Aliseda *et al.* 2002; Hill 2005), direct numerical simulations (DNSs) (Wang & Maxey 1993) and theory (Dávila & Hunt 2001). The effect is substantial for order one microscale Stokes and settling parameters (Wang & Maxey 1993). The numerical simulations of Yang & Lei (1998), however, have also shown this effect to be strongly dependent on the large eddies.

Settling velocity reduction may be achieved for small, tracer-like particles by vortex trapping (Manton 1974; Tooby, Gerald & John 1977), by nonlinear drag for large, heavy particles (Mei 1994) or by the loitering effect. The loitering effect, as described by Nielsen (1993), occurs when the turbulence is weak relative to the particle Stokes velocities and thus the particles fall too quickly through the flow field to react to the eddies and spend more time on average in upward-moving regions of the flow. This may result in a mean settling velocity reduction of up to 40 % when compared with a particle's Stokes velocity (Nielsen 1993). Experiments (Murray 1970; Nielsen 1993; Kawanisi & Shiozaki 2008) have shown the relevant parameter to be $Sv_\ell$. Transition from settling enhancement to reduction occurs in the $Sv_\ell$ range $10^{-1}$–$10^{0}$, with the critical value varying with Stokes number (Kawanisi & Shiozaki 2008). When the $Sv_\ell$ number is sufficiently large, there is a return to the quiescent terminal velocity.

Our droplets are too heavy to undergo vortex trapping and are generally too small to undergo nonlinear drag due to either large Reynolds numbers or significant deformation, with only the largest droplets having particle Reynolds numbers based

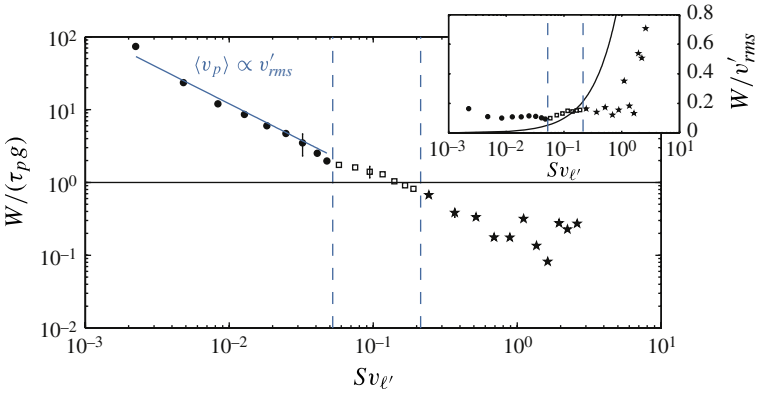


FIGURE 7. (Colour online) Settling velocity enhancement versus settling parameter, $Sv_\ell$, in the homogeneous, high-turbulence side of the flows with homogeneous particle seeding. Black circles, open squares and stars represent the small, intermediate and large droplet groups, respectively. The inset shows the settling velocity normalized by $v'_{rms}$. The black line shows the droplet Stokes velocities.

on slip velocity (approximated as $Re_p \approx \tau_p g d/\nu$) greater than order $10^{-1}$, or droplet Weber numbers ($We \equiv \rho_p v_{St}^2 d/\sigma$, $\sigma$ being the surface tension) greater than order $10^{-2}$. The droplet $Sv_\ell$ range, however, is sufficient for both enhancement of the small droplet settling velocities by the fast-tracking mechanism and reduction of the large droplet settling velocities due to the loitering effect. This is shown in figure 7, where, following the Nielsen (1993) scaling, the settling velocity ($W$) enhancement is plotted as a function of $Sv_\ell$ in the homogeneous region. (Whereas Nielsen (1993) adjusted turbulence levels in a flume seeded with monodispersed particles, in the present study we observe polydispered particles in a shared turbulent flow.) Clearly, the measurements show a transition from settling enhancement to reduction to occur in the $Sv_\ell$ range of $10^{-1}$–$10^0$, and this is in agreement with Kawanisi & Shiozaki (2008).

To the best of the authors' knowledge, this is the first report of the loitering effect in wind tunnel turbulence. The loitering effect has been largely overlooked outside the fields of sedimentation and hydrology. For small $Sv_\ell$, the turbulence is strong relative to the particle Stokes velocities. The settling speed of these particles is insensitive to differences in Stokes velocities, and is instead proportional to the velocities of the eddies which fast-track them. This is further illustrated in the inset to figure 7, where $W/v'_{rms}$ is shown to be approximately constant up to $Sv_\ell \sim 1$. From the inset, $W/v'_{rms} \approx 0.1$, but there was variation between data sets, with some showing a proportionality constant closer to 0.2, although the same trend. These values are within the range documented by Kawanisi & Shiozaki (2008). (The rising velocities of $\lambda$-scale, buoyant particles has also been shown by Friedman & Katz (2002) to be proportional to 25 % of the turbulence r.m.s. velocity, regardless of Stokes number variation.) For the large $Sv_\ell$ droplets in our flow (the scatter is due to the relatively low numbers of these droplets), there is the expected increase in $W$, although it always remains less than the droplet Stokes velocities ($\tau_p g$), as is clear from both the main figure and the Stokes velocities line in the inset.

The large-scale settling parameter, $Sv_\ell \equiv \tau_p g/v_{rms}$, may alternatively be expressed as $Sv_\ell \equiv \tau_\ell/(\ell/\tau_p g)$, the ratio of the characteristic time of a large eddy to the time for a particle travelling at its Stokes velocity to pass it, and the same interpretation is true for $Sv_\eta$ and the interaction of particles with smaller eddies. Particles which fall

| Study | Present | Kawanisi & Shiozaki (2008) | Aliseda *et al.* (2002) | Wang & Maxey (1993) | Yang & Shy (2005) |
|---|---|---|---|---|---|
| Type | Active grid | Flume & KS | Passive grid | DNS | FWM |
| $Re_\lambda$ | 275 | *N/A* | 75 | 20–60 | 73–202 |
| $u_{rms}/u_\eta$ | 8 | *N/A* | 2.8–3.7 | 2.3–4.3 | 4.4–7.2 |
| $\ell/\eta$ | 600 | *N/A* | 180–205 | 21–33 | 43–83 |
| $d$ (μm) | 5–75 | 40–600 | 5–50 | *N/A* | 12–40 |
| $St_\eta$ | 0.007–6 | *N/A* | 0.01–5 | 1–2.7 | 0.36–1.9 |
| $Sv_\eta$ | 0.02–15 | *N/A* | $10^{-4}$–0.014 | 0.4–4 | 0.9–6 |
| $St_\ell$ | $10^{-4}$–0.08 | 0.0003–0.06 | $10^{-3}$–0.1 | 0.002–0.012 | 0.01–10.4 |
| $Sv_\ell$ | $10^{-3}$–2.5 | 0.05–5 | <0.005 | 0.1–1.7 | 0.12–1.4 |

TABLE 3. Comparison with studies on particle settling. Values are approximate, and for the present study reflect the full range shown in figures 7 and 8. In the flume studies showing bifurcated settling effects (Nielsen 1993; Kawanisi & Shiozaki 2008), we note that the turbulence r.m.s. was estimated from the particle r.m.s. velocities, which is reasonable for scaling purposes. Those statistics which are either not available or not applicable are listed as '*N/A*'. For Kawanisi & Shiozaki (2008), KS stands for kinematic simulation. FWM denotes 'French washing machine', a general description of the air turbulence experimental apparatus of Yang & Shy (2005).

too quickly through the flow field to effectively preference the downward-sweeping sides of eddies will experience a net reduction in their mean settling velocity, spending more time 'loitering' in upward-moving regions of the flow than they do 'fast-tracking' through downward-moving regions. Looking again to the figure 7 inset and the black line representing the Stokes velocities, it is clear that as a result of both the fast-tracking and loitering effects, the range of settling velocities observed for the droplet distribution is much diminished from what is predicted by Stokes drag.

Table 3 compares our parameter range with studies focused on particle settling. It is evident that there is large scale separation, $(\ell/\eta)'$, in the intense turbulence of the present flow. This is particularly true when compared with the well-known DNS study of Wang & Maxey (1993), but also with the experiments of Yang & Shy (2005). Particle loitering was not observed in Yang & Shy (2005), which has a similar $Sv_\ell$ range to the present study, but also much greater $St_\ell$ values. Our large-scale droplet parameters are comparable with the flume study of Kawanisi & Shiozaki (2008). The settling parameters in our flow are considerably larger than in the passive grid turbulence study of Aliseda *et al.* (2002), while the droplet parameters are comparable in general with Wang & Maxey (1993).

### 3.3. *The droplet mixing layers*

We now turn to the particles in the inhomogeneous conditions of the droplet mixing layers, addressing both their mean droplet number density profiles and r.d.f.s. While the mean number density profiles describe the droplet mixing layers by their mean quantities, the r.d.f.s measure how the droplets are spatially distributed. We show that the mean droplet number density ($n$) evolves analogously to the (Fickian) diffusion of a concentration species. This is the case for both the TTI and TNI, despite the large-scale intermittency of the TNI. We also show the effect of the entrainment on the r.d.f.s, and lay the groundwork for the proceeding sections.

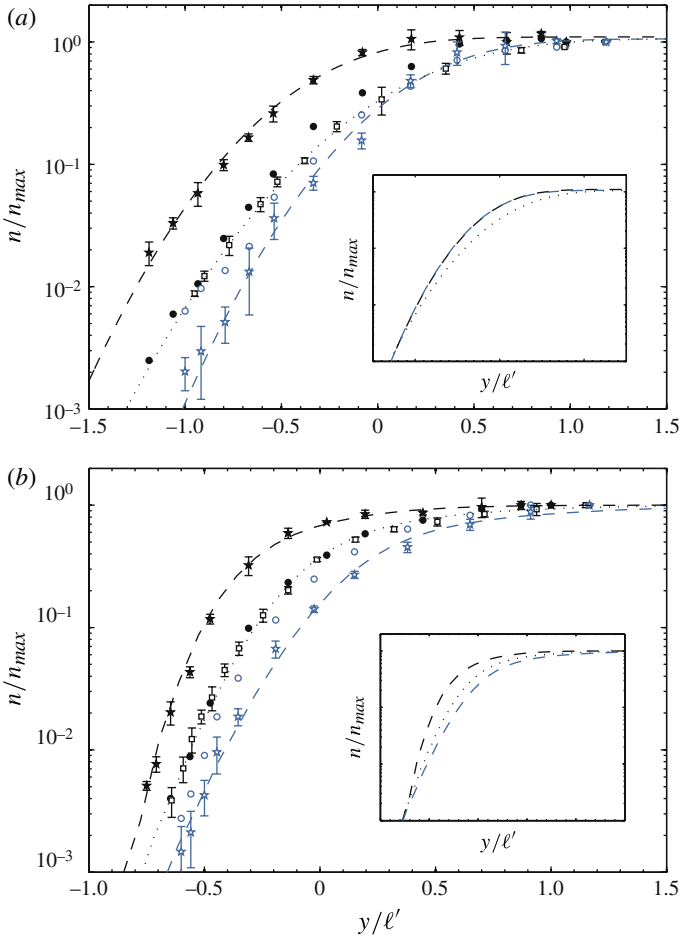


FIGURE 8. (Colour online) Droplet number density profiles for the TTI (*a*) and TNI (*b*). Circles and stars denote the small and large droplet groups, respectively, for both the $g+$ (filled symbols) and $g-$ (open symbols) cases. Open squares denote the $g0$ small droplet case. Lines are error function fits for the TTI and finite-element method (FEM) fits for the TNI (see the text); the insets show the main figure fits shifted to converge asymptotically.

3.3.1. *Mean droplet number density profiles*

The mean droplet number density ($n$) profiles for the large and small droplet groups are shown for the TTI and TNI cases in figure 8. (The droplet number density is determined from the linear density of droplets measured by the PDPA, and normalized by the maximum value at that downstream location, $n_{max}$. Figure 4 of GGW shows profiles from the same data sets for the full distribution and for droplets with $d \geqslant 50$ μm.) There are two important aspects: the shape of the profiles and their relative positions (abscissa).

The mean droplet number density profiles for the TTI case are error functions (as reported in GGW). This indicates that for the TTI, $n$ evolves to first-order like any concentration species does from a step initial condition in a domain with a homogeneous diffusivity. The TNI case by contrast is strongly inhomogeneous, and so error function profiles of $n$ are neither expected nor observed. The TNI $n$ profiles

(figure 8*b*) are overlaid with solutions from a simple, advection–diffusion model for $n$ in a domain with variable (turbulent) diffusivity (as opposed to the homogeneous diffusivity of the TTI mixing layer), which is described in appendix A. The purpose of the model is to demonstrate what properties of the droplet mixing layers can be easily modelled, despite a number of simplifying assumptions and the complexities of both turbulent entrainment and multiscale turbulence. It is evident from the fits that the time evolution of the mean quantity $n$ may be captured by a simple advection–diffusion model for the TNI, just like for the TTI.

The insets to figure 8 show the main figure fits artificially shifted to converge at the tails. Since the first-order effect of the particle settling on the $n$ profiles (as a function of droplet size) is a lateral shift, we take their shape to be indicative of the turbulent mixing alone. Here, 'mixing' is defined for the mean particle number density analogously as for a diffusive scalar, that is, as the ability of the flow and mean number density gradients to cause the mean number density field to become more uniform. A droplet mixing layer with a more gradual fall-off in its mean droplet number density is hence more effectively 'mixed' than one with a steeper fall-off and narrower interface, regardless of abscissa. We see in the insets that there is some discernable change in the profile shapes for the large droplets with gravity as compared with the small droplet and $g0$ cases. The large droplet cases have a sharper fall-off in $n$ for the TTI and TNI $g+$ cases, but not for the TNI $g-$ case. The more gradual fall-off in $n$ for the TNI $g-$ large droplet case can be explained by the fact that its droplets are shifted further into the high-turbulence side of the TNI. The large droplet $g0$ case has been omitted to avoid clutter. It was shown in GGW that for the $g0$ cases $n$ is insensitive to droplet size, and thus that the large scales which do not effectively discriminate between the droplets due to their inertia (see $St_{\ell'}$ in table 2), dominate the entrainment. From the inset to figure 8(*a*), however, it is apparent that the turbulent mixing may be sensitive to $Sv_\ell$ when gravity is directed across the interface, with the droplet number density effective diffusivities being diminished for the large droplets with gravity.

The relative shifting of the $n$ profiles (figure 8) is of the order expected from gravitational settling (GGW). Apart from this, however, we also observed comparable shifts due to slight difference in the initial conditions for the flows, and these are discussed in appendix B. Valid comparisons of the profile abscissae may still be made within a given flow case, however. For example, the shift between the small and large droplet number density profiles is relatively small for the TTI $g-$ case as compared with the TTI $g+$ case. This indicates the broken symmetry of gravity aiding versus inhibiting the droplet transport.

### 3.3.2. *Droplet r.d.f.s and conditional number densities*

The r.d.f. is the established measurement of particle clustering, and is defined as the average density of the particles in a volume shell/slice at a fixed distance from a central particle, normalized by the mean density of the particles in the domain (McQuarrie 1976). Both the r.d.f., $g(r)$, and related pair correlation function, $h(r) \equiv g(r) - 1$, have been used to study the inertial clustering of heavy particles in homogeneous turbulence (e.g. Sundaram & Collins 1997; Wood *et al.* 2005; Saw *et al.* 2008; Salazar *et al.* 2008). The r.d.f. is of particular interest in cloud physics because it contains vital information for predicting particle collisions (Shaw, Kostinski & Larsen 2002; Shaw 2003). (Shaw *et al.* 2002 computed the pair correlation function for droplets both within a cloud and for traverses including ambient air). The 1D r.d.f. is defined as $g(r) \equiv (N_r/\delta r)/(N/L)$ (e.g. Holtzer & Collins 2002), that is, the

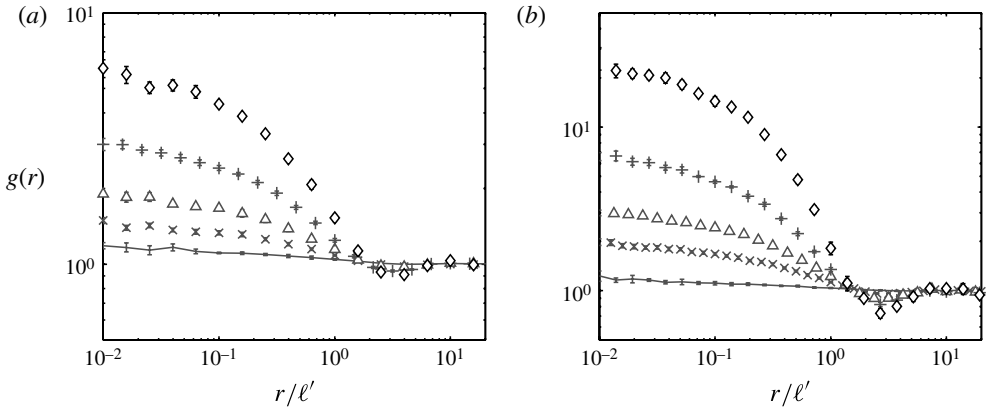


FIGURE 9. Radial distribution function, $g(r)$, for the $g+$ case with small droplets for the TTI ($a$) and TNI ($b$). The measurement locations are at $y/\ell' = 1, 1/4, 0, -1/4$ and $-1/2$ for the TTI and $y/\ell' = 5/6, 0, -1/6, -1/3$ and $-1/2$ for the TNI, denoted by the solid line, $\times$, $\triangle$, $+$ and $\diamond$, respectively.

average number of particle pairs with separation distance $r$, ($N_r$, with a bin width of $\delta r$), normalized by the mean droplet linear number density, $n \equiv N/L$. The droplet separations were determined using Taylor's hypothesis and the Eulerian PDPA data.

The important features of our r.d.f.s did not differ qualitatively between the flow (TTI and TNI) and gravitational cases, nor between the droplet groups (except that the r.d.f.s are sensitive to the relative positions of the mean number density profiles of figure 8). Figure 9 thus shows r.d.f.s for the $g+$ small droplets only, as they are most numerous and their statistical error is lowest. Looking at the seeded region, ($y/\ell' \approx 1$), $g(r)$ is relatively uniform. This is particularly true for the small droplets, whose $St_\eta$ (table 2) is too small for significant, small-scale inertial clustering. For the large droplets (not shown), the values do tend to increase for very small $r$, consistent with their order one $St_\eta$ (Saw *et al.* 2008). Moving across the droplet mixing layers to negative $y/\ell'$, the magnitude of $g(r/\ell' < 1)$ increases strongly and monotonically, consistent with the decreasing mean number densities (figure 8). There is however a sharp decrease with $r$ in the r.d.f. through $r/\ell' \approx 1$. This indicates that the droplets are organized into integral-scale clusters. There is a dip in $g(r)$ at $r/\ell' \approx 2$ to subunity values which grows across the mixing layers. This dip is a result of the droplet-free gaps between the large-scale clusters. It is useful to refer back to the figure 1 image, imagining the turbulent bursts to be droplet-laden. The 1D $g(r)$ functions measure the droplet spatial distribution along lines tracing horizontally through the flow. The large-scale clustering is indicated where the lines trace through alternating droplet-free and droplet-laden regions of fluid. Since droplet-laden large scales penetrate both the TTI and the TNI, the large-scale clusters result for both, despite the absence of large-scale intermittency in the TTI velocity field. By clustering, we simply mean the state of the particle field as being spatially correlated rather than randomly distributed. While the large-scale clusters might be expected (and a passive scalar would likely behave in a similar way to the particles), it is not entirely obvious since it is not clear how the time scale of the formation of such clusters compares with that of their breakup/dispersion as a result of the ambient turbulence.

The large-scale clusters are observed for both the small and large droplet groups. Unlike for inertial clustering, large-scale clusters due to entrainment should persist

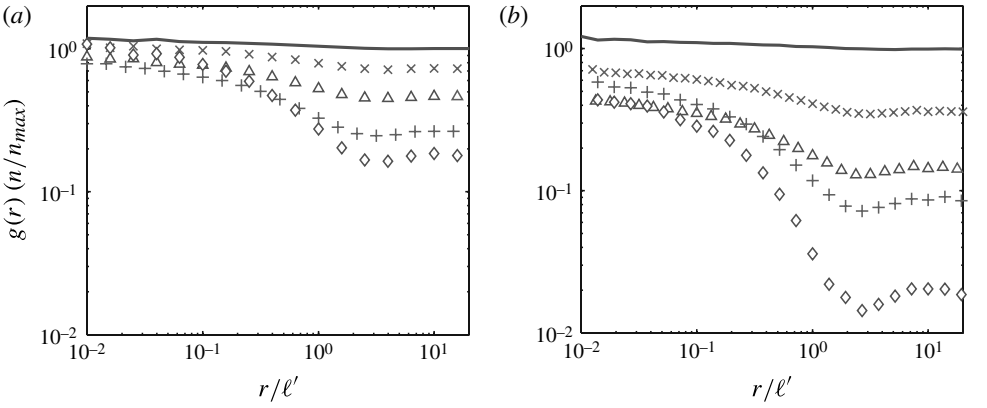


FIGURE 10. Product $g(r) \cdot (n/n_{max})$ for the $g+$ case small droplets for the TTI (*a*) and TNI (*b*). The measurement locations are at $y/\ell' = 1, 1/4, 0, -1/4$ and $-1/2$ for the TTI and $y/\ell' = 5/6, 0, -1/6, -1/3$ and $-1/2$ for the TNI, denoted by the solid line, $\times$, $\triangle$, $+$ and $\diamond$, respectively.

as $St \to 0$. In fact, the mechanism should only be less effective for very heavy particles as $St, Sv \to \infty$, since such particles may not effectively follow turbulent bursts across the interface. We expect some differences in the clustering for the large and small droplet groups in the presence of gravity due to their $Sv_\ell$ values (table 2). This is difficult to determine with our r.d.f.s, however, since the two droplet groups can have very different local mean number densities in the gravitational cases.

The sharp increases in $g(r)$ for $r/\ell' < 1$ (figure 9) are clearly due to the declining mean number densities (figure 8), but the question remains as to whether the properties within the large-scale clusters remain unchanged. While figure 9 presents the r.d.f.s in the typical fashion, it is instructive in our case to correct for the mean number density differences at each $y/\ell'$ location by multiplying the r.d.f.s by $n/n_{max}$. This is done in figure 10, which allows us to see the density changes in the mixing layers of droplet pairs with various separation distances. The values at the right end of the $r/\ell'$ axes in figure 10 show the local mean number density (since $\lim_{r\to\infty} g(r) = 1$), while the values on the left extreme ($r/\ell' \ll 1$) essentially show the droplet densities within the large-scale clusters. While the droplet mean number densities at $y/\ell' = -1/2$ are one and two orders of magnitude less than that in the source region for the TTI and TNI (figure 8), respectively, the droplet densities within the large-scale clusters only appear to be diminished by tens of percents. The droplet densities are thus largely preserved within the large-scale clusters in the entrainment zone.

Figure 11 shows conditioned profiles of the mean droplet number densities for the TTI and TNI $g0$ cases; the unconditioned mean number density profiles are also shown for comparison. For the conditioned profiles, the large, droplet-free spaces in the droplet measurement time series are ignored in calculating the mean number densities. These spaces are identified using a threshold value of the largest droplet separations in the seeded side of the flows, where there are no large-scale droplet clusters. The conditional profiles show that the droplet number densities within the large-scale clusters vary far less than the mean number densities, confirming the results of figure 10. The profiles also indicate that the conditional densities for the TNI are in fact higher than for the TTI, which is opposite to the case for the mean profiles.

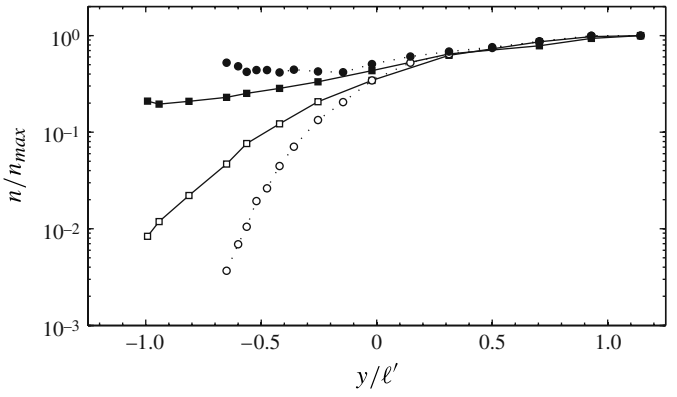


FIGURE 11. Conditional (filled symbols) and regular (open symbols) mean droplet number density profiles for the TTI (squares) and TNI (circles) $g0$ cases. The unconditioned profiles are the same as in figure 8.

This is due to the nature of the entrainment mechanism. The droplets are entrained in droplet-laden, large-scale clusters which break up and disperse over time such that the droplets become more uniformly distributed. The ambient turbulence of the TTI aids in this dispersal, while the quiescent conditions of the TNI allow the clusters to endure. We also note that the conditional profiles are not monotonic in $y$, and this fits with our description of the entrainment. The growing droplet mixing layer introduces droplets to previously droplet-free regions via the clusters described above. The clusters in the low-mean-density, 'growth' region have shorter regional time histories than those in the central portion of the mixing layer, since the growth region has only clusters which have recently penetrated to their current position. These droplet clusters have had little time to break up and disperse, and so it is possible for the droplets and turbulence within them to retain a state more similar to the source region than to the 'dispersed', or mixed region in between, where the large-scale clusters have had time to break up are less dense on average. In figure 11, we may then identify the growth regions by their increase in the cluster-conditioned droplet densities. These regions roughly correspond to where the unconditioned droplet mean number density $n/n_{max} \lesssim 10^{-2}$. Referring back to figure 10, we note that the $(n/n_{max})g(r/\ell' \ll 1)$ values were similarly non-monotonic in $y$.

### 3.4. *Droplet entrainment and velocity statistics*

In this section we examine the droplet entrainment using their velocity data. In particular, we examine the role of the mean number density gradients and large-scale clustering on the mean droplet velocities and the moments of the velocity distributions.

#### 3.4.1. *Droplet mean velocities and transport*

Mean droplet velocity $(-V_p)$ profiles are shown in figure 12. Clearly, the mean velocities increase across the mixing layers for both the small and large droplet groups and all flow cases. In GGW we could not discern velocity differences between the $g+$ and $g-$ cases due to poorer resolution of the velocity data. Here, we discern the velocity differences between the small and large droplets; the difference is generally smaller than that predicted by the droplet group Stokes velocities ($\Delta Sv_{\ell'} \equiv \Delta\tau_p g/v'_{rms} \approx 0.3$, table 2), consistent with the turbulence settling effects

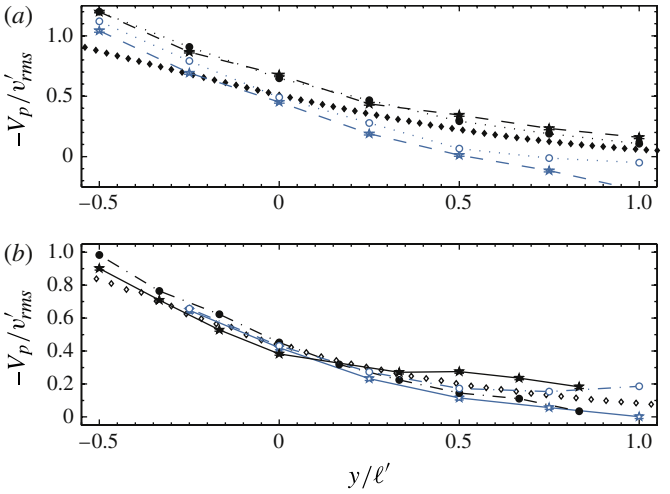


FIGURE 12. (Colour online) TTI (*a*) and TNI (*b*) mean transverse droplet velocity profiles across the mixing layers. Circles and stars denote small and large droplet groups, respectively, for both the $g+$ (filled symbols) and $g-$ (open symbols) cases. The small and large droplet groups are further distinguished by dotted and dashed lines for the TTI, and mixed-dashed and solid lines for the TNI. Filled and open diamonds, for the TTI and TNI, respectively, show the expected mean velocity based on a Fickian mixing model and the $g0$ number density profile fits of figure 8. The error bars shown here and for figures 14–15 are 95 % confidence intervals, and in some cases are similar in size to the data point symbols. They are shown only for the (less numerous) large droplet data to avoid clutter.

described in § 3.2.2. We note that in figure 12 there is a crossing of the large- and small-droplet velocity profiles for the TNI $g+$ case. The other flow case velocity profiles also show a tendency to converge (at large negative $y$), but they are not seen to cross. There are two mechanisms by which these trends may result; the first relates to gradient-driven transport and may result in crossing, and the second to the intermittent penetration of the large scales across the interfaces.

The crossing of mean velocity profiles is expected when the mean velocity is tied to gradients in the local number density field, as it is in Fickian mixing. If the droplet field shifts due to gravitational settling, so do the velocity profiles. In this scenario, a shift in abscissa for a given droplet group due to gravitational settling has an effect opposite to that of the particle settling velocity on the local mean velocity. This is perhaps best understood in the following way: if a particle $g0$ case has number density $n_0(y,t)$ and mean velocity profile $V_0(y,t)$, where $t$ is the advection time from the initial condition ($t=0$), then, to first order, the $g+$ case has $n_+(y,t) = n_0(y+Wt,t)$ and $V_+(y,t) = V_0(y+Wt,t) + W$, where $W$ is the particle settling velocity. While the $W$ term increases the mean velocity uniformly, the downstream shift in abscissa ($Wt$) moves the gravity case down the $V_0$ curve for a local velocity reduction. Eventually, a crossover in the mean velocities due to differences in $W$ for two differing particle groups is expected. This is quite clear for the TNI $g+$ case. Here, we see that the tails of the large and small droplet number density profiles (figure 8) are separated by $y/\ell' \sim 0.2$ near $y/\ell' = -0.5$. In figure 12, such a shift in abscissa corresponds to a velocity reduction for the TNI $g+$ large particles of $V_p/v' \sim 0.3$, which is similar to the change in the large versus small droplet group $V_p$ difference between this location ($y/\ell' = -0.5$) and the homogeneous region ($y/\ell' \approx 1$).

Owing to the configuration of the wind tunnel, we were only able to measure the transverse velocity for the $g+$ and $g-$ cases. In order to further examine the degree to which the mean droplet transport is gradient-driven, the theoretical mean droplet velocities based on a purely Fickian mixing model are also plotted in figure 12 based on the $g0$, small droplet group number density profile fits (figure 8). For the TTI case this has the analytic form

$$V_p(x, y) \equiv -\frac{D_n}{n}\frac{\partial n}{\partial y} = -\sqrt{\frac{D_n U}{\pi x}}\frac{\exp(-(y-y_o)^2/(4D_n(x/U)))}{1+erf((y-y_o)/\sqrt{4D_n(x/U)})}. \tag{3.1}$$

The Fickian model velocities do not account for changes in $V_p$ due to particle settling. The model profiles are however similar in shape to the measured profiles, although for the TTI the model values increase more slowly across the interface than do the measurements. The agreement is particularly good for the TNI. We note that the TTI cases have greater mean droplet velocities in general.

For the TTI, and the TNI $g-$ case, the velocity difference between the droplet groups narrows across the particle mixing layers, but the profiles do not cross. The degree to which this is a result of the shifting effect described above is unclear, as there is a second mechanism for the convergence. Figure 13 shows the mean velocity of the droplets conditioned on and as a function of the distance, $r$, between adjacent droplets (based on interarrival times). This is shown at $y/\ell' = -1/4$, where figure 9 demonstrated high degrees of large-scale droplet clustering. It is clear that the droplets which travel fastest across the interfaces are also those which are most densely grouped (small $r/\ell'$). The fast-moving, dense droplet clusters are swept unidirectionally by the large scales from the seeded region and thus have the greatest mean velocities. Since the flux, $J$, of particles with separation distance $r$ goes as $J(r) \propto V_p(r) \times r^{-3}$ (since the volumetric number density goes as $r^{-3}$), it is clear from figure 13 that the droplet-laden bursts dominate the particle entrainment. We note that the mean velocity differences between the droplet groups and gravitational cases in figure 13 become negligible for small $r/\ell'$, as velocities for clustered droplets within intermittent bursts are determined by the fluid burst velocities and are less sensitive to the mean droplet number density gradients. Thus, as we traverse the particle mixing layers from positive to negative $y$, where there is progressively more large-scale clustering, we expect both the convergence of the velocity profiles and the departure from the Fickian model lines (figure 12).

3.4.2. *Moments of the droplet velocity distributions*

Figure 14 shows the droplet velocity r.m.s. profiles for the $v$ component, normalized by $v'_{rms}$. We note that the profiles were qualitatively the same for the $u$ component, and that when compared with the fluid velocity hot wire measurements, the particle r.m.s. velocities were greater by $\sim$10 and 20 % in the homogeneous region for the $u$ and $v$ components, respectively, presumably reflecting the way the particles sample the fluid. Moving across the particle mixing layers, there is a decrease in the droplet velocity r.m.s. for even the TTI case, which has transversely homogeneous turbulence. In general, particles which sample a fluid velocity probability density function (p.d.f.) should see a decrease in their velocity r.m.s. when there is a mean number density gradient. Here, however, the situation is complicated by the bursting.

In the entrainment region, there are both droplets which have crossed the interfaces well upstream of the test section and have had time to disperse and adjust to the local fluid velocity field, and still densely clustered droplets recently ejected in bursts from the seeded region. The velocities of such bursts are associated with those of

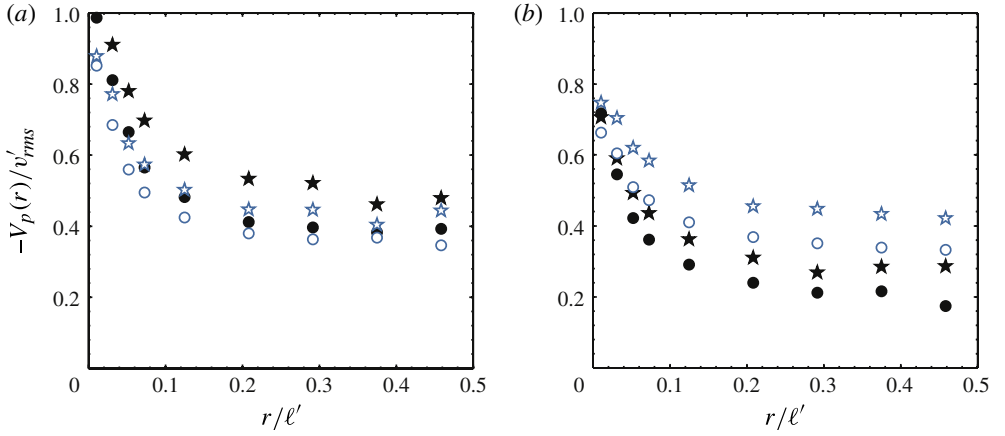


FIGURE 13. (Colour online) TTI (*a*) and TNI (*b*) mean droplet velocity as a function of local droplet separation distance, $r$, for the $g+$ (filled symbols) and $g-$ (open symbols) cases. Circles and stars denote the small and large droplet groups at $y/\ell' = -1/4$.

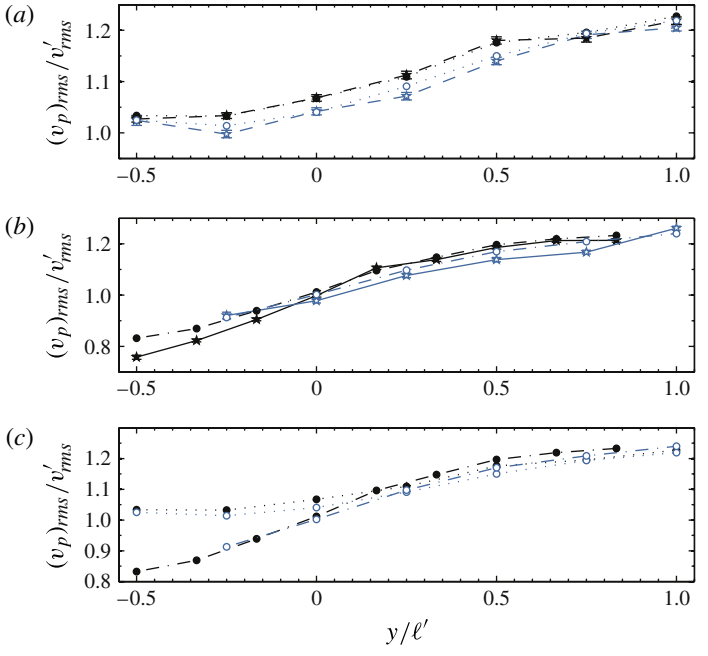


FIGURE 14. (Colour online) TTI (*a*) and TNI (*b*) droplet $(v_p)_{rms}$ profiles across the mixing layers. Circles and stars denote the small and large droplet groups, respectively, for both the $g+$ (filled symbols) and $g-$ (open symbols) cases. The small and large droplet groups are further distinguished by dotted and dashed lines for the TTI, and mixed-dashed and solid lines for the TNI. The small droplet TTI and TNI cases are also shown together for comparison (*c*).

the tail of the high-turbulence fluid velocity p.d.f. (in the seeded side of the flows). It is expected then that the droplet velocity r.m.s. contribution from the variance of these burst velocities thus declines as one moves across the particle mixing layers to where only successively stronger bursts can penetrate, and droplets are observed to be

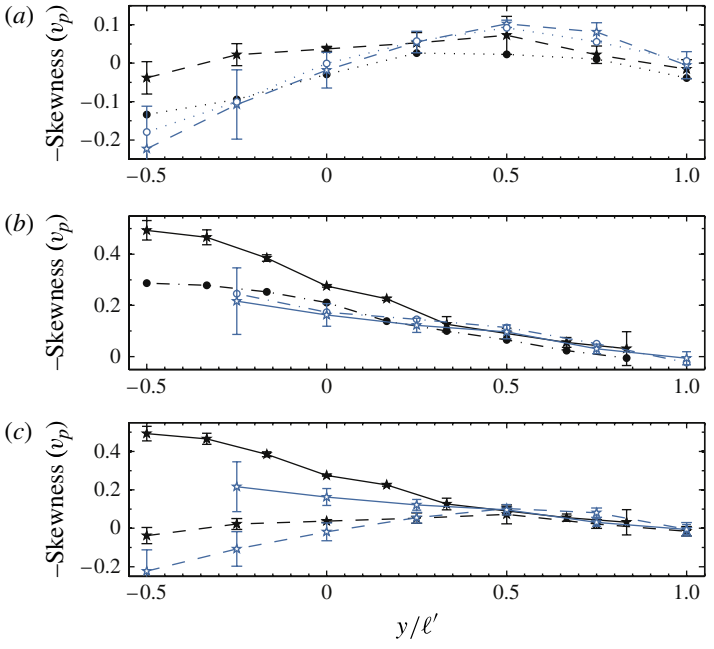


FIGURE 15. (Colour online) TTI (*a*) and TNI (*b*) droplet velocity skewness profiles across the mixing layers. Circles and stars denote the small and large droplet groups, respectively, for both the $g+$ (filled symbols) and $g-$ (open symbols) cases. The small and large droplet groups are further distinguished by dotted and dashed lines for the TTI, and mixed-dashed and solid lines for the TNI. The large droplet TTI and TNI cases are also shown together for comparison (*c*).

increasingly clustered at the large scales. As expected, there is a greater reduction in the droplet velocity r.m.s. for the TNI than for the TTI, due to the sampling of the low-turbulence fluid velocity field, and possibly more invariant penetration of the fluid bursts into relatively quiescent rather than highly turbulent fluid.

The differences in the droplet velocity r.m.s. profiles between the droplet groups or gravitational cases are small. In general, however, we expect the droplet velocity statistics to be more reflective of the fluid velocity field where the droplets are least clustered at the large scales, where their mean number density is relatively high. For the TTI and the high-turbulence side of the TNI, the velocity field has a higher r.m.s. than that we expect is associated with the bursting droplets. Here, the $g+$ droplets have higher velocity r.m.s. than do the $g-$ droplets, consistent with their greater number density which better reflects the fluid velocity field. For the TNI there is a switch near $y/\ell' \approx 0$. The fluid velocity field r.m.s. becomes very small through this region (figure 3), and we see that the TNI $g+$ droplet velocity r.m.s. becomes reduced as compared with the TNI $g-$ droplet cases. While the differences in the measurements presented in figures 14 and 15 are small (although confirmed by the confidence intervals), the trends are remarkably consistent with the DNS results of an analogous mixing layer by Ireland & Collins (2011).

Figure 15 shows the (negative) droplet velocity skewness, such that we may refer to the velocity being skewed with (positive values) or against (negative values) the mean transport direction. In the homogeneous regions ($y/\ell' = 1$), the droplet velocity skewness is nearly zero for both the TTI and TNI, like for the fluid velocity fields.

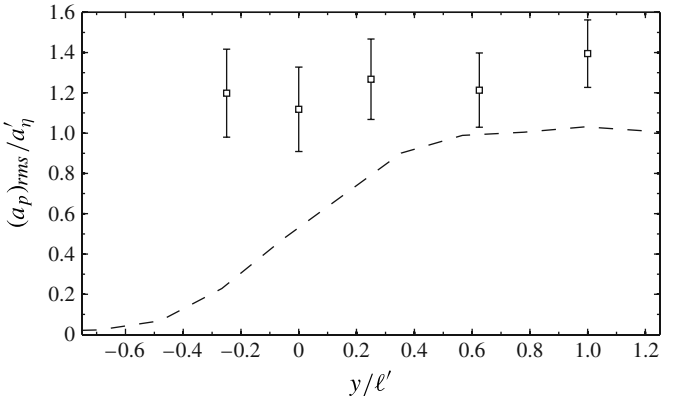


FIGURE 16. Profile of the droplet acceleration r.m.s. (symbols) for the full droplet size distribution ($g0$ case) in the TNI. The streamwise acceleration data is shown. The dashed line shows the variation of the Kolmogorov acceleration, $a_\eta \equiv (\epsilon^3/\nu)^{1/4}$, as determined from the mean dissipation profile for the TNI (figure 3).

Proceeding into the mixing layers where there is little or no large-scale clustering ($0.5 < y/\ell' < 1$, figure 9), the skewnesses become weakly positive. For $y/\ell' < 0.5$, the droplet velocity skewness continues to grow positively for the TNI cases, while it decreases and becomes weakly negative for the TTI cases.

The moments of the droplet velocity p.d.f.s indicate how the droplets sample the fluid velocity field. Although the TTI velocity field is unskewed, figure 13 clearly shows that the droplets in the bursting region heavily sample the high-velocity events that are in the positive tail of the fluid velocity p.d.f. As a result, the TTI particle velocity p.d.f.s in the bursting region have elongated negative tails and negative skewnesses. For the TNI, the droplets sample a velocity field which is largely positively skewed (figure 5) due to its large-scale intermittency, and the droplet velocity distributions reflect this skewness. Although the shape of the droplet number density profiles certainly has some effect on the droplet velocity statistics, the measurements are very consistent in light of the clustered entrainment. Those droplet groups and flow cases which show comparatively more large-scale clustering at a particular $y/\ell'$ location (see figure 9), also have more negative transverse droplet velocity ($v_p$) skewness. Where the mean number densities are higher, the $v_p$ skewness is more positive and closer to the velocity field values (figure 5). We lastly note that the skewed p.d.f.s also have super-Gaussian values of kurtosis, with values reaching $\sim 4$ at $y/\ell' = -0.5$ for the TNI $g+$ large droplets, and $\sim 3.5$ for the other cases.

### 3.5. *Droplet accelerations*

We have thus far documented the large-scale entrainment and clustering of water droplets in both the TTI and TNI. Given the results of GGW, this has helped explain the absence of evaporative effects without a full description of the humidity field and its correlation to the droplet field. While the only distinguishing factor between the air flows on either side of the TTI may be its vapour content, for the case of the TNI, the turbulence levels are also quite distinct. In this final section we look at the droplet accelerations, which, being indicative of the small scales of the turbulence, give us insight into the particle–fluid interactions in the entrainment zone.

Figure 16 shows a profile of the droplet acceleration r.m.s. in the TNI. The full distribution $g0$ data is shown, as the Lagrangian particle tracking system is unable to discern particle sizes, and the particle size distribution is not a function of $y$ in the $g0$ case (GGW). While the dashed line shows the variation of the Kolmogorov eddy acceleration, $a_\eta \equiv (\epsilon^3/\nu)^{1/4}$, based on the TNI mean dissipation profile (figure 3), the symbols show measurements of the droplet r.m.s. accelerations. The streamwise component is shown, although the measurements are not strongly sensitive to this choice. We take the r.m.s. values to be the proper scale of the droplet accelerations, as the mean accelerations are zero in the shearless interfaces. The large error bars are due to the pixel-limited spatial resolution of the particle tracking system.

Clearly, the droplet accelerations do not differ substantially across the TNI, despite the large step in the turbulence levels. This indicates that the turbulence within the bursts and large-scale droplet clusters is similar to that in the high-turbulence, droplet-laden side of the flows. This is like in the droplet-free, figure 1 image. Since the sub-Kolmogorov-sized droplets only feel the small scales of the turbulence, and these small scales do not differ within the fluid bursts which transport the bulk of the droplets, the particle–fluid interactions remain only weakly changed in even the TNI. Measurements in the gravitational cases at $y/\ell' = \pm 1/4$ also showed only small differences in the acceleration r.m.s., although these differences were also consistent with changes in the droplet size distributions due to gravity (see GGW). The acceleration measurements are thus consistent with the general results of the present study, that the intermittent entrainment mechanism preserves the droplet-ambient conditions that are present in the injection side of the flows.

## 4. Conclusions

We have studied the entrainment of inertial particles across two shearless interfaces. Water droplets injected into the turbulent side of the flows were entrained into a coflow that was in one case close to laminar (TNI) and in another having the same turbulence characteristics as the droplet carrier flow (TTI). The effects of gravity were isolated by turning the apparatus with respect to the gravitational field. The study followed from the earlier work of Gerashchenko *et al.* (2011), which focused mainly on the mean droplet statistics. Here, we have studied higher-order statistics as well as particle pair and Lagrangian acceleration data.

Our main findings are as follows. In homogeneous conditions, the polydispersed droplets (ranging in size from a few micrometres to approximately 80 μm, figure 6) were shown to exhibit both enhanced and reduced settling velocities (compared with their Stokes velocities in a quiescent flow), depending on their large-scale settling parameter, the ratio of the characteristic time of an eddy to the time for a particle travelling at its Stokes velocity to pass it (§ 3.2.2). While the small particles fell faster than their Stokes velocities in a quiescent flow due to their preference for the downward-sweeping sides of eddies, the large droplet settling velocities were reduced due to droplets loitering in upward-moving regions of the flow. This 'loitering' effect appears not to have been previously reported in wind tunnel experiments.

In the particle mixing layers of the TTI and TNI, the mean particle transport velocities increased across the entrainment region for all particle sizes and for gravity both aiding and inhibiting the mixing process ($g+$ and $g-$, figure 12). Consistent with the turbulence settling effects, the differences in the mean velocities of the large and small droplets was smaller than predicted from their Stokes velocities. For the $g+$, TNI case, there was a crossing of the large and small droplet velocity profiles,

with the small droplets travelling faster than the larger ones far into the entrainment region. This was attributed mainly to the shifting of the mean number density profiles relative to each other due to gravitational settling (§ 3.4.1). Convergence of the velocity profiles in this region was observed for the other cases. While the relative shifting of the number density profiles may be partially responsible for this convergence, conditional velocity statistics (figure 13) showed that the turbulent bursts which transport most droplets are insensitive to droplet size and gravitational case, and thus, that the convergence is expected by this intermittent entrainment mechanism. Still, a Fickian, mean-gradient mixing model was able to capture the form of the mean velocity profiles, particularly for the TNI case (figure 12). The droplet r.m.s. velocities decreased across the entrainment region for both the TNI and TTI, although this was less pronounced for the latter (figure 14). The ability of a burst of droplets to penetrate deeply into the entrainment region depends on its energy, and thus the droplet velocity probability distributions narrow across the particle mixing layers. The skewness of the droplet velocity distributions was also documented (figure 15), showing that the droplets in regions with more pronounced large-scale clustering also exhibit more negative (counter-entrainment) velocity skewness.

The droplet r.d.f.s were used to show the droplet spatial organization throughout the flows. Radial distribution functions have traditionally been used to show small-scale (inertial) clustering in isotropic particle fields, where inertial particles are centrifuged out of the regions of high vorticity into regions of high strain (Shaw *et al.* 1998). Here, we have shown the large-scale clustering of droplets due to the intermittent entrainment process. This clustering was evident in the velocity fields of not only the inhomogeneous TNI, but the homogeneous TTI as well (figure 9). The large-scale clustering presented in increased magnitudes in the r.d.f.s for $r/\ell' < 1$ and decreased magnitudes for order one $r/\ell'$, representing the droplet-free gaps between large-scale clusters.

At the small scales, there was little change in the nature of the r.d.f.s as compared with in the homogeneous, droplet-laden side of the flows. Thus, the bursting associated with the entrainment appears not to affect the small-scale clustering. Lagrangian measurements of the droplet accelerations (figure 16) also showed little change in this small-scale quantity for even the strongly inhomogeneous TNI velocity field. The ability of the entrainment process to transport large, macroscale bursts without affecting the small-scale properties is consistent with the earlier finding of GGW, that the droplet size distribution does not change across the interfaces for the $g0$ cases, in which gravity does not play a role (GGW, figure 5*a*). The lack of a change in the particle size distribution for the $g0$ cases indicates that the large-scale bursts transport the droplet-laden fluid in bulk. Evaporative effects thus appear to be negligible in our flows. Conditional statistics of the mean droplet number densities (figure 11) showed that, as may be expected, the large-scale clusters were more dense in the TNI than for the TTI, where the background turbulence is more effective in dispersing the particles. Both the conditional statistics and the r.d.f.s provided information on the time histories of the large-scale droplet clusters. In particular, the droplet-laden bursts which have penetrated farthest across the growing mixing layers may have properties more similar to their source region than to the intermediate, centre portion of the mixing layer (figure 11 and related discussion). In this central region, droplet clusters transported earlier by smaller turbulence scales will have had more time to break up and disperse, and their droplets will be more uniformly distributed and less dense as a result (§ 3.3.2).

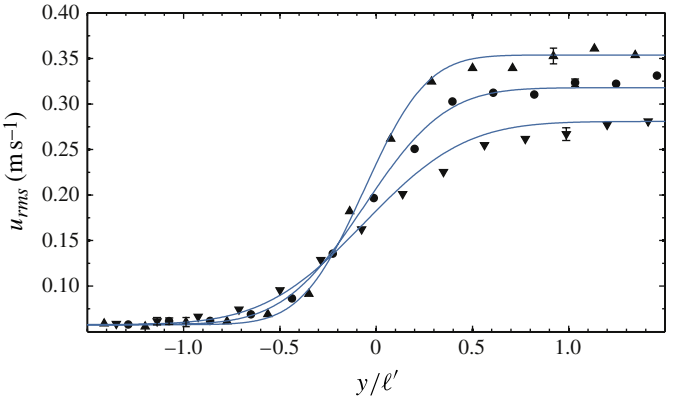


FIGURE 17. (Colour online) TNI profiles of $u_{rms}$ upstream ($t/\tau_{\ell'} \approx 0.4$, $x = 0.7$ m), downstream ($t/\tau_{\ell'} \approx 1.1$, $x = 1.8$ m) and at the test section ($t/\tau_{\ell'} \approx 0.7$, $x = 1.20$ m), denoted by upward- and downward-pointing triangles and circles, respectively. The form of the error functions plotted at each $x$ location is discussed in appendix A.

The experiments help in our understanding of cloud boundaries, whether they be at the floors, sides or ceilings of clouds. As noted in GGW, the experimental parameters (with the exception of the low Reynolds numbers) are in the range observed in typical cumulous clouds (Siebert *et al.* 2010). The $Sv_\ell$ range of the experiment (0.03–0.35) and clouds ($10^{-3}$–$10^{0}$) is noteworthy, as some micrometeorological models which neglect the role of turbulence in droplet coalescence and cloud evolution rely on Stokes velocity differences between large and small droplets (Shaw 2003), which may actually be diminished due to turbulence. The results relate more broadly to particle entrainment in environmental flows, like the atmospheric boundary layer, as well as to industrial and energy-related applications concerned with the mixing or dispersion of heavy particles.

## Acknowledgements

We thank P. Ireland and L. Collins for their discussion, and refer the reader to Ireland & Collins (2011) for a comparison of the results with DNS studies. We also thank T. Cowen for the use of the Defrees Hydraulics Lab wind tunnel. This work was supported by the US National Science Foundation.

## Appendix A. The TNI droplet mixing layer model

Here, we describe the simple advection–diffusion model used for the TNI droplet mixing layer, where the droplet mean number density is treated like a diffusive species and hot-wire data has been used to inform a domain with an inhomogeneous turbulent diffusivity. We begin with the downstream evolution of the $u_{rms}$ profiles for the TNI case in figure 17. These are approximately error functions, so we first model the $u_{rms}$ evolution as a diffusive process as well. The form of the error functions plotted in figure 17 is determined from the analytical solution to the 1D advection–diffusion equation of a concentration species with step initial condition in a domain with homogeneous diffusivity, $D$. In a high-Péclet-number regime in two dimensions, where an advective scale ($U$) dominates the diffusive scale, the Taylor approximation $t = x/U$

may be used. The profiles were fit with the adapted form

$$u_{rms}(x, y) = u'_{min} + \left(\frac{u'_{max} - u'_{min}}{2}\right)\left[1 + erf\left(\frac{y - y_o}{\sqrt{4D_u(x/U)}}\right)\right], \tag{A 1}$$

where $u'_{min}$, $u'_{max}$, $y_o$ and $D_u$ are fitting parameters, the former two being the asymptotic $u_{rms}$ values for a given error function fit. The three $u_{rms}$ profiles are reasonably well-approximated using a constant diffusivity, $D_u$, of the turbulence r.m.s. Since $u'_{max} \propto (x_g)^{-m/2}$, where $x_g$ is the distance from the active grid and with $m$ the turbulence decay constant (e.g. Comte-Bellot & Corrsin 1971), and since the other parameters did not vary significantly between fits at different downstream locations, the mixing layer $u_{rms}$ may be approximated by a single equation in two dimensions. (We note that while the TTI droplet number density error function fits mentioned in the text indicate that the turbulence decay is not of primary importance, since they indicate a homogeneous diffusivity, we have chosen here to model the TNI flow profiles with the decay, as they were measured.) The figure 17 fits are calculated based on this single equation, and it is apparent that the TNI $u_{rms}$ evolution may be modelled in this manner. Given $D_n \propto u_{rms}\ell$ (where $D_n$ is the diffusivity of the droplet number density), $\ell \propto (x_g)^{1-m/2}$ (disregarding its transverse variation) and the previous result for $u_{rms}(x, y)$, $D_n(x, y)$ may be modelled to within a constant of proportionality. Using this, a simple, steady-state advection–diffusion finite-element model was created with a two-dimensional spatial domain, where a concentration species representing $n$ advects/diffuses from a stepped boundary condition. (The mean streamwise velocity is input into the model.)

The resulting model fits were thus determined for figure 8(*b*). We note that the model constants produced diffusivities ($D_n$) in agreement with those of the TTI figure 8(*a*) error function fits (of the form of (A 1)), but that these were nearly an order of magnitude smaller than predicted by the $u_{rms}\ell$ scaling, and this may be indicative of stirring/entrainment at the subintegral scales.

## Appendix B. The role of initial conditions

As mentioned in the text, there is some shifting of the mean droplet number density profiles due to experimental initial conditions. This is known in particular from the $g0$ cases, where for the TTI the inflection point of the mean droplet number density profile (an error function) is displaced from $y = 0$, and for the TNI, where the profile is found to be yet further displaced when compared with matching profiles from both our model (appendix A) and the DNS results of an analogous mixing layer by Ireland & Collins (2011). The causes of these shifts may be: (i) a deficit in the mean droplet number density near the splitter plate at the initial condition for both the TTI and TNI (due to the reduced particle flux in the spitter plate boundary layer); and (ii) the flow asymmetry for the TNI. Figure 18(*a*) shows the droplet number density initial condition, which is not perfectly (uniformly) mixed before the end of the splitter plate by the grid turbulence. A TTI diffusion model, a simplified version of that described for the TNI in appendix A, was used to show anticipated number density profiles resulting from both a uniform initial condition and one with a linear deficit. The resultant profile is the same in shape, but there is a shift of abscissa on the order of the number density displacement thickness of the deficit, and this result has been confirmed with the help of DNS (Peter Ireland, private communication). We find the TTI and TNI $g0$ cases to be shifted by $\sim$5 and $\sim$8 cm into the turbulent, seeded region, respectively. The additional displacement in the TNI case could be

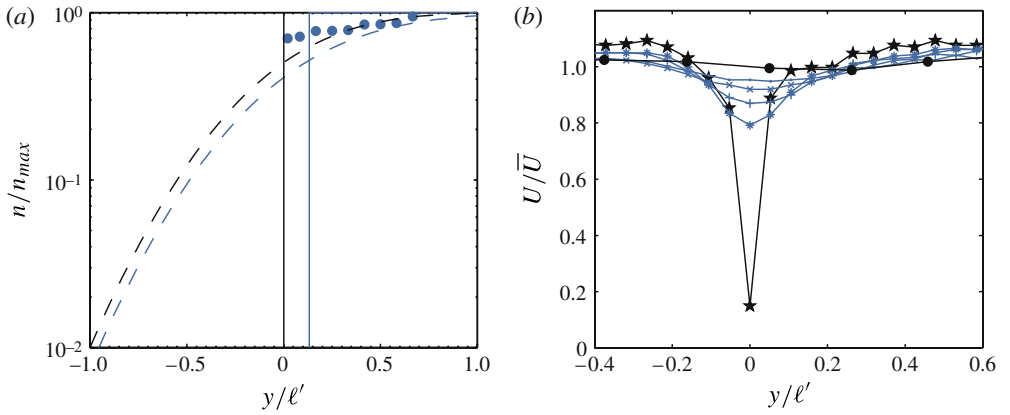


FIGURE 18. (Colour online) Mixing layer displacements due to the droplet mean number density initial condition (at $x \equiv 0$) (*a*) and the diffusion of the splitter plate momentum deficit (*b*). In (*a*), the circles are the measured initial condition; the vertical line ($y/\ell' \approx 0.13$) denotes the *displacement thickness* of the number density profile. The dashed lines are FEM solutions (see appendix A) for the test section based on a uniform profile and one with a linear deficit matched to the measured profile. In (*b*), hot-wire mean velocity profiles (normalized by the average velocity at their respective downstream location) are shown between the splitter plate trailing edge and the test section. Measurement stations are at $t/\tau_{\ell'} \approx 0.003, 0.064, 0.186, 0.427, 0.611$ and 0.7, where $t = x/U$, denoted by stars, asterisks, pluses, multiplication signs, dots and circles, respectively.

explained by more efficient mixing of the momentum deficit from the splitter plate boundary layers into the high-turbulence side, as shown in the hot-wire wake profiles of figure 18(*b*).

## REFERENCES

ALISEDA, A., CARTELLIER, A., HAINAUX, F. & LASHERAS, J. C. 2002 Effect of preferential concentration on the settling velocity of heavy particles in homogeneous isotropic turbulence. *J. Fluid Mech.* **468**, 77–105.

ANDREJCZUK, M., GRABOWSKI, W. W., MALINOWSKI, S. P. & SMOLARKIEWICZ, P. K. 2004 Numerical simulation of cloud clear air interfacial mixing. *Atmos. Sci.* **61**, 17261739.

AYYALASOMAYAJULA, S., GYLFASON, A., COLLINS, L. R., BODENSCHATZ, E. & WARHAFT, Z. 2006 Lagrangian measurements of inertial particle accelerations in grid generated wind tunnel turbulence. *Phys. Rev. Lett.* **97**, 144507.

BEC, J., BIFERALE, L., CENCINI, M., LANOTTE, A., MUSACCHI, S. & TOSCHI, F. 2007 Heavy particle concentration in turbulence at dissipative and inertial scales. *Phys. Rev. Lett.* **98**, 084502.

BROADWELL, J. E. & BREIDENTHAL, R. E. 1982 A simple model of mixing and chemical reaction in a turbulent shear layer. *J. Fluid Mech.* **125**, 397–410.

COMTE-BELLOT, G. & CORRSIN, S. 1971 Simple eulerian time correlation of full and narrow-band velocity signals in grid-generated 'isotropic' turbulence. *J. Fluid Mech.* **48**, 273–337.

DÁVILA, J. & HUNT, J. C. R. 2001 Settling of small particles near vortices and in turbulence. *J. Fluid Mech.* **440**, 117–145.

DEARDORFF, J. W. 1974 Three-dimensional numerical study of turbulence in an entraining mixed layer. *Boundary-Layer Meteorol.* **7** (2), 199–226.

FRIEDMAN, P. D. & KATZ, J. 2002 Mean rise rate of droplets in isotropic turbulence. *Phys. Fluids* **14**, 3059–3073.

GERASHCHENKO, S., GOOD, G. & WARHAFT, Z. 2011 Entrainment and mixing of water droplets across a shearless turbulent interface with and without gravitational effects. *J. Fluid Mech.* **668**, 293–303.

GERASHCHENKO, S., SHARP, N. S., NEUSCAMMAN, S. & WARHAFT, Z. 2008 Lagrangian measurements of inertial particle accelerations in a turbulent boundary layer. *J. Fluid Mech.* **617**, 255–281.

HILL, R. J. 2005 Geometric collision rates and trajectories of cloud droplets falling into a burgers vortex. *Phys. Fluids* **17**, 037103.

HOLTZER, G. L. & COLLINS, L. R. 2002 Relationship between the intrinsic radial distribution function for an isotropic field of particles and lower-dimensional measurements. *J. Fluid Mech.* **459**, 93–102.

IRELAND, P. J. & COLLINS, L. R. 2011 Direct numerical simulation of inertial particle entrainment in a shearless mixing layer. *J. Fluid Mech.* (submitted).

JAYESH, & WARHAFT, Z. 1994 Turbulent penetration of a thermally stratified interfacial layer in a wind tunnel. *J. Fluid Mech.* **277**, 23–54.

KANG, H. S. & MENEVEAU, C. 2008 Experimental study of an active grid-generated shearless mixing layer and comparisons with large-eddy simulation. *J. Fluid Mech.* **20**, 125102.

KANTHA, L. H., PHILLIPS, O. M. & AZAD, R. 1977 On turbulent entrainment at a stable density interface. *J. Fluid Mech.* **79**, 753–768.

KAWANISI, K. & SHIOZAKI, R. 2008 Turbulent effects on the settling velocity of suspended sediment. *J. Hydraul. Engng ASCE* **134** (2), 261–266.

LÁZARO, B. J. & LASHERAS, J. C. 1989 Particle dispersion in a turbulent, plane, free shear layer. *Phys. Fluids* **1**, 1035–1044.

LONGMIRE, E. K. & EATON, J. K. 1992 Structure of a particle-laden round jet. *J. Fluid Mech.* **236**, 217–257.

MANTON, M. J. 1974 On the motion of a small particle in the atmosphere. *Boundary-Layer Meteorol.* **6**, 487–504.

MCQUARRIE, D. A. 1976 *Statistical Mechanics*. Harper Row.

MEI, R. 1994 Effect of turbulence on the particle settling velocity in the nonlinear drag range. *Intl J. Multiphase Flow* **20**, 273–284.

MORDANT, N., CRAWFORD, A. & BODENSCHATZ, E. 2004 Experimental Lagrangian acceleration probability density function measurements. *Physica* D **193**, 245–251.

MURRAY, S. P. 1970 Settling velocities and vertical diffusion of particles in turbulent water. *J. Geophys. Res.* **75**, 1647–1654.

MYDLARSKI, L. & WARHAFT, Z. 1996 On the onset of high-Reynolds-number grid-generated wind tunnel turbulence. *J. Fluid Mech.* **320**, 331–368.

NIELSEN, P. 1993 Turbulence effects on the settling of suspended particles. *J. Sedim. Petrol.* **63** (5), 835–838.

OUELLETTE, N. T., XU, H., BOURGOIN, M. & BODENSCHATZ, E. 2006 A quantitative study of three-dimensional Lagrangian particle tracking algorithms. *Exp. Fluids* **40**, 301–313.

SALAZAR, J. P. L. C., DE JONG, J., CAO, L., WOODWARD, S. H., MENG, H. & COLLINS, L. R. 2008 Experimental and numerical investigations of inertial particle clustering in isotropic turbulence. *J. Fluid Mech.* **600**, 245–256.

SAW, E. W., SHAW, R. A., AYYALASOMAYAYAJULA, S., CHUANG, P. Y. & GYLFASON, Á. 2008 Inertial clustering of particles in high-Reynolds-number turbulence. *Phys. Rev. Lett.* **100**, 214501.

SHAW, R. A. 2003 Particle-turbulence interactions in atmospheric clouds. *Annu. Rev. Fluid Mech.* **35**, 183–227.

SHAW, R. A., KOSTINSKI, A. B. & LARSEN, M. L. 2002 Towards quantifying droplet clustering in clouds. *Q. J. R. Meteorol. Soc.* **128** (582), 1043–1057.

SHAW, R. A., READE, W. C., COLLINS, L. R. & VERLINDE, J. 1998 Preferential concentration of cloud droplets by turbulence: effects on the early evolution of cumulus cloud droplet spectra. *J. Atmos. Sci.* **55**, 1965–1976.

SIEBERT, H., GERASHCHENKO, S., GYLFASON, A., LEHMANN, K., COLLINS, L. R., SHAW, R. A. & WARHAFT, Z. 2010 Towards understanding the role of turbulence on droplets in clouds: in situ and laboratory measurements. *Atmos. Res.* **97**, 426–437.

SQUIRES, K. D. & EATON, J. K. 1991 Preferential concentration of particles by turbulence. *Phys. Fluids* A **3**, 1169–1178.

SUNDARAM, S. & COLLINS, L. R. 1997 Collision statistics in an isotropic particle-laden turbulent suspension. Part 1. Direct numerical simulations. *J. Fluid Mech.* **335**, 75–109.

TOOBY, P. F., GERALD, L. W. & JOHN, D. I. 1977 The motion of a small sphere in a rotating velocity field: a possible mechanism for suspending particles in turbulence. *J. Geophys. Res.* **82** (15), 2096–2100.

TOWNSEND, A. A. 1976 *The Structure of Turbulent Shear Flow*. Cambridge University Press.

TURNER, J. S. 1986 Turbulent entrainment: the development of the entrainment assumption, and its applications to geophysical flows. *J. Fluid Mech.* **173**, 431–471.

VEERAVALLI, S. & WARHAFT, Z. 1989 The shearless turbulence mixing layer. *J. Fluid Mech.* **207**, 194–229.

VOTH, G. A., PORTA, A. LA, CRAWFORD, A. M., ALEXANDER, J. & BODENSCHATZ, E. 2002 Measurement of particle accelerations in fully developed turbulence. *J. Fluid Mech.* **469**, 121–160.

WANG, L. P. & MAXEY, M. R. 1993 Settling velocity and concentration distribution of heavy particles in homogeneous isotropic turbulence. *J. Fluid Mech.* **256**, 26–68.

WOOD, A. M., HWANG, W. & EATON, J. K. 2005 Preferential concentration of particles in homogeneous and isotropic turbulence. *Intl J. Multiphase Flow* **31**, 1220–1230.

YANG, C. Y. & LEI, U. 1998 The role of turbulent scales in the settling velocity of heavy particles in homogeneous isotropic turbulence. *J. Fluid Mech.* **371**, 179–205.

YANG, T. S. & SHY, S. S. 2005 Two-way interactions between solid particles and homogeneous air turbulence: particle settling rate and turbulence modification measurements. *J. Fluid Mech.* **526**, 171–216.